Numerical investigations of small-amplitude disturbances in a boundary layer with impinging shock wave at $Ma=4.8$

Alessandro Pagella,[a] Ulrich Rist, and Siegfried Wagner
Institut für Aero- und Gasdynamik, Universität Stuttgart, 70550 Stuttgart, Germany

(Received 12 October 2001; accepted 1 April 2002; published 20 May 2002)

The stability behavior of a laminar boundary layer with shock boundary layer interaction and small amplitude disturbances is investigated by linear stability theory and direct numerical simulation. By a complex interaction of several physical properties, the impinging shock wave locally influences stability behavior of the boundary layer, dependent on its shock strength, applied disturbance frequency, and disturbance propagation angle with respect to the flow direction (obliqueness angle). Due to the displacement of the boundary layer near shock impingement and the according Reynolds number effect in this area, the boundary layer is locally destabilized. The displacement of the boundary layer also produces an increase of the thickness of local regions of relative supersonic speed, which promotes second mode instability. For the results obtained by direct numerical simulation nonparallel effects could be identified and quantified. Taking these nonparallel effects into account, linear stability theory is able to represent the stability behavior of wall distant disturbance amplitude maxima having small obliqueness angles for the cases investigated here. For larger obliqueness angles and disturbance amplitudes at or close to the wall the agreement between linear stability theory and direct numerical simulation declines considerably. © *2002 American Institute of Physics.* [DOI: 10.1063/1.1480265]

I. INTRODUCTION

Laminar-turbulent transition is of crucial importance for super- and hypersonic aircraft. Transition to turbulence yields considerable aerodynamic loads. Especially under super- and hypersonic conditions, transition is not sufficiently investigated, so far. However, a good insight into hypersonic transition is given by Saric, Reshotko, and Arnal.[1]

The first phase of transitional development, the amplification of small amplitude disturbances can be described by linear stability theory. Today's investigations of compressible, small amplitude disturbance behavior are based on the work done by Mack,[2] who considerably extended the pioneering works of Lees and Lin.[3] Lees and Lin carried out a detailed study of the inviscid theory. They classified the disturbances into subsonic, sonic and supersonic disturbances and found a sufficient condition for the presence of subsonic, amplified disturbances in the existence of a generalized inflection point. This point is located in the boundary layer, where the gradient of the product of density and the wall-normal derivative of the mean flow velocity is zero. A compressible boundary layer on an insulated flat plate always has such a generalized inflection point and consequently is unstable to inviscid disturbances. These subsonic disturbances can be characterized as vorticity waves and will be referred to as first mode instabilities further on. Also for infinite Reynolds numbers at first, Mack proved, that additional neutral solutions exist. These higher modes, acoustic in origin, occur when a region of relative supersonic flow is present in the boundary layer, i.e., when the disturbance phase velocity is supersonic compared to the wall-nearest boundary layer flow. For a boundary layer on an insulated wall, this is the case for Mach numbers larger than $Ma \approx 2.2$. The higher modes represent sound waves reflecting from the wall and the relative sonic line.[2] The first of these higher modes (often labeled as ''Mack Modes''), called ''second mode,'' is of great importance at high Mach numbers, because of its large amplification rates. The higher modes are most amplified for two-dimensional disturbance waves. First mode disturbances dominate at low supersonic Mach numbers and can be stabilized by cooling, suction or a favorable pressure gradient. Second mode instabilities behave in a different manner, however. Suction and a favorable pressure gradient leads to a stabilization of the boundary layer, but cooling destabilizes it. For finite Reynolds numbers, viscosity is destabilizing at low Mach numbers. Also, inviscid instability is weak and the stability behavior is mainly dominated by viscous instability. In contrast, at higher Mach numbers the effect of viscosity is stabilizing and inviscid instability picks up, becoming dominant at $Ma \approx 3.8$.

Shock boundary layer interaction has been a major research topic over the last decades as well. It is a crucial physical phenomenon which occurs in an almost infinite number of applications of external and internal flows relevant to aircraft, rockets and projectiles. First systematic experimental studies on laminar and turbulent boundary layers interacting with shock waves where done by Ackeret, Feldmann, and Rott[4] as well as Liepmann.[5] For aircrafts flying under super- or hypersonic conditions shock boundary layer interaction is an important occurrence. It causes undesired effects such as local heat peaks, high aerodynamic loads,

[a]Telephone: (+49)(0)711-6853429; fax: (+49)(0)711-6853438; electronic mail: pagella@iag.uni-stuttgart.de

increase of drag and jet intake performance loss, to name only a few. A sufficiently strong shock wave causes the boundary layer to separate. The high pressure rise at separation yields compression waves, forming the so-called separation shock, which interacts with the impinging shock wave well outside the boundary layer. The impinging shock wave penetrates into the boundary layer where it ends at the sonic line and from where it is reflected as a system of expansion waves. On its way from the outflow to iso-Mach line $Ma=1$, the shock angle gets steeper. The compression waves associated with reattachment coalesce to the reattachment shock. A comprehensive introduction into shock boundary layer interactions of all kinds can be found in Ref. 6; more recent summaries in Refs. 7 and 8. According to Ref. 8 important quantities like peak heating in strong interactions or unsteady pressure peaks still cannot be predicted very accurately or even not at all due to restrictions in computational and measurement capabilities, especially for complex geometries and flow fields.

The work done for this paper wants to merge the two single research topics explained above, namely transitional behavior of a laminar boundary layer at $Ma=4.8$ with impinging shock wave, which is of high scientific and practical interest, as it was remarked, e.g., in Ref. 8. So far, no scientific publications of work done on such transitional interactions are known to the authors. Within this paper, we investigate the first phase of the transition process, the linear regime. In the following section, an introduction to the numerical scheme is given. Next, a discussion of the base-flow properties for various shock strengths follows. The next section focuses on linear stability theory investigations. Finally, results from direct numerical simulations are discussed and a conclusion and an outlook to future research is given.

II. NUMERICAL SCHEME

The numerical scheme, which is based on the works of Thumm,[9] Eißler,[10–12] and Fezer[13] was extended by Pagella[14,15] to investigate shock boundary layer interactions. A two-dimensional base flow is calculated by solving the two-dimensional Navier–Stokes equations. After obtaining a steady state from the two-dimensional equations, the three-dimensional solver uses the steady solution as start-up data. In contrast to the two-dimensional scheme, the three-dimensional one is formulated in disturbance-flow formulation. The difference between both formulations is, that certain steady terms of the Navier–Stokes equations do not have to be recalculated for each time step with the disturbance-flow formulation.[10] However, this is applicable for weak shocks only, because a larger shock angle tends to cause a highly unsteady flow, even without artificial disturbances. The investigation of the stability behavior, regarding an unsteady shock boundary layer situation is, therefore, beyond the scope of the present investigations, but part of planned future work. The investigations within this paper are limited to relatively weak shocks, yielding two-dimensional steady base flows.

A. Governing equations

The numerical scheme is based on the complete, unsteady, three-dimensional Navier–Stokes equations in Cartesian coordinates for compressible flows in conservative formulation

$$\frac{\partial p}{\partial t}+\nabla\cdot(\rho\mathbf{u})=0, \tag{1}$$

$$\frac{\partial(\rho\mathbf{u})}{\partial t}+\nabla\cdot(\rho\mathbf{uu})+\nabla\mathbf{p}=\frac{1}{\mathrm{Re}}\nabla\cdot\sigma, \tag{2}$$

$$\frac{\partial(\rho e)}{\partial t}+\nabla\cdot(p+\rho e)\mathbf{u} =\frac{1}{(\kappa-1)\mathrm{Re}\,PrMa^2}\nabla\cdot(\vartheta\nabla T)+\frac{1}{\mathrm{Re}}\nabla\cdot(\sigma\mathbf{u}), \tag{3}$$

where

$$\sigma=\mu[(\nabla\mathbf{u}+\nabla\mathbf{u}^{\mathbf{T}})-\tfrac{2}{3}(\nabla\cdot\mathbf{u})\mathbf{I}], \tag{4}$$

with the velocity vector $\mathbf{u}=[u,v,w]^T$ and

$$e=\int c_v dT+\tfrac{1}{2}(u^2+v^2+w^2). \tag{5}$$

We assume a nonreacting, ideal gas with constant Prandtl number $Pr=0.71$ and specific heat ratio $\kappa=c_p/c_v=1.4$. c_p and c_v are the specific heat coefficients under constant pressure and constant volume, respectively, which follow $c_p-c_v=R$, with the universal gas constant R.

For temperatures $T>T_s$, viscosity is calculated by the Sutherland law

$$\frac{\mu}{\mu_\infty}=\left(\frac{T}{T_\infty}\right)^{3/2}\frac{T_\infty+T_s}{T+T_s},\quad T_s=110.4\,\mathrm{K}, \tag{6}$$

while for temperatures below T_s, the relation $\mu/\mu_\infty=T/T_\infty$ is used.[16] The thermal conductivity coefficient in Eq. (3) $\vartheta=c_p\mu_\infty/Pr$ is proportional to the viscosity.

For the simulations, lengths are nondimensionalized by a reference length L, which appears in a global Reynolds number $\mathrm{Re}=\rho_\infty * u_\infty * L/\mu_\infty=10^5$. Because it is common use in linear stability theory to apply a Reynolds number scaled with the displacement thickness, which is proportional to $\sqrt{x}$, we introduce a local Reynolds number $R_x=\sqrt{x*\mathrm{Re}}$, as well. Time t is normalized by the ratio L/u_∞, where u_∞ is the free-stream velocity, while the specific heat c_v is normalized with u_∞^2/T_∞ (T_∞ denotes free-stream temperature). Density ρ, temperature T and viscosity μ are standarized by their respective free-stream values.

B. Integration domain

Figure 1 shows the integration domain. The calculation starts at x_0, the end of the integration domain is given by x_N. x_s gives the location of the shock, which is prescribed at the free-stream boundary, according to the Rankine–Hugoniot relations.[17] A buffer domain[18] can be switched on at x_3, which is damping the disturbances in order to provide an undisturbed, laminar flow at the outflow boundary. The disturbance strip is located between $x_1\leqslant x\leqslant x_2$, with R_{x_1}

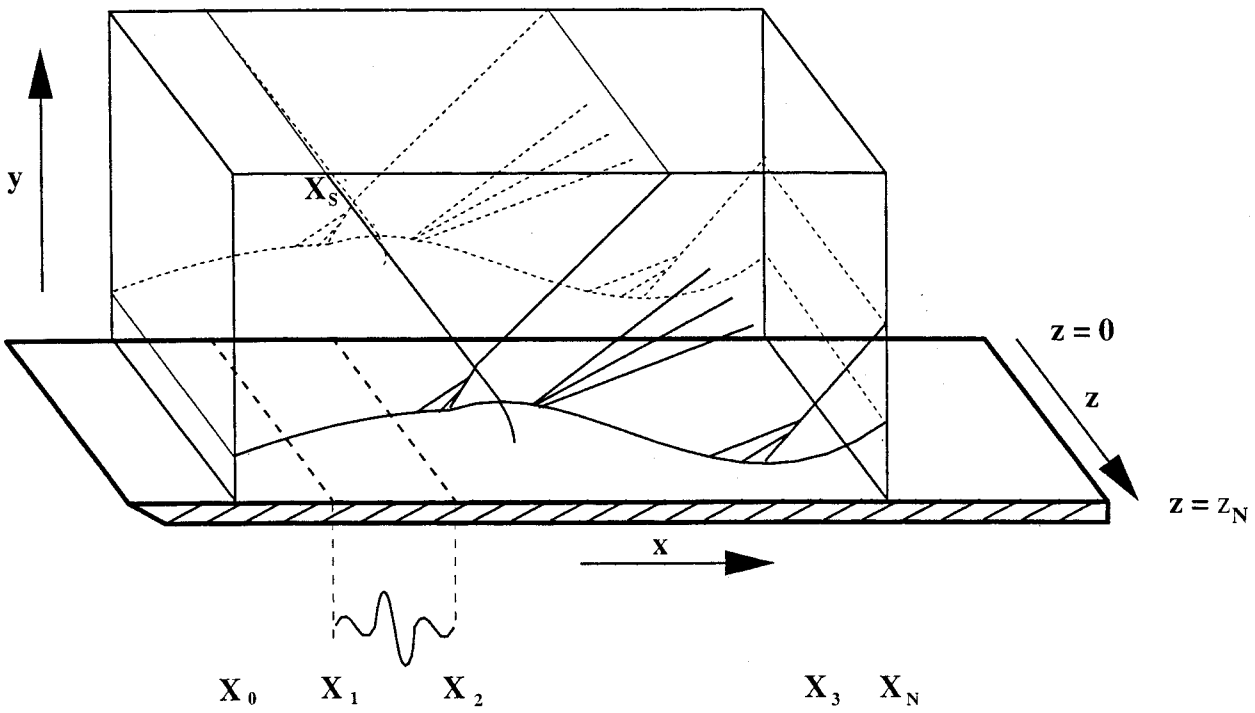

FIG. 1. Integration domain and disturbance strip.

$=438$ and $R_{x_2}=952$. The disturbances are periodic in spanwise direction, having a wavelength of λ_z, which determines the width of the integration domain as $z_N=\lambda_z$.

C. Discretization

Due to the specific characteristics of the solution in different spatial directions, the discretization is specific to each spatial direction, accordingly. We assume a numerical grid with $N*M$ gridpoints in streamwise and wall normal direction, as well as K-harmonics in spanwise direction, respectively. In streamwise direction the solution has a wave character in the presence of disturbance waves which are either amplified or damped. Compact finite differences are able to resolve this kind of solution in an appropriate manner. They are applied here in a split-type form.[19] This split-type formulation has some desired damping characteristics with respect to small-scale oscillations. In wall-normal direction split-type finite differences of fourth order accuracy are used to calculate convective terms, while viscous terms are calculated by fourth-order central differences. In spanwise direction we have periodic boundaries, which allow to apply a spectral approximation with Fourier expansion.[20] Time integration is performed at equidistant time steps with a standard Runge–Kutta scheme of fourth-order accuracy. A more thorough discussion of the numerical scheme can be found in Ref. 10. To summarize, the formal accuracy of the scheme is (Δx^{4-6}, Δy^4, Δt^4, z spectral).

D. Filter

Test computations have shown that the above discretization reliably works for oblique shocks in the computation of the base flow, as long as the step sizes are fine enough. Typical step sizes in streamwise and wall-normal directions are $\Delta x=0.0357$, $\Delta y=0.005\,25$, respectively. However, as the shock approaches the sonic line in the boundary layer it turns towards a vertical shock normal to the plate and oscillations in streamwise direction occur around the shock wave because of insufficient resolution in x direction. Without further grid refinement or damping, these oscillations may destroy the numerical solution. To stabilize the computation, a fourth-order accurate filter according to Lele[21] is used

$$\alpha\hat{f}_{i-1}+\hat{f}_i+\alpha\hat{f}_{i+1}=af_i+\frac{c}{2}(f_{i+2}+f_{i-2})+\frac{b}{2}(f_{i+1}+f_{i-1}), \tag{7}$$

where variables marked as $\hat{f}_i$ denote filtered and f_i unfiltered values at gridpoint i in x direction with

$$a=\tfrac{1}{8}(5+6\alpha), \quad b=\tfrac{1}{2}(1+2\alpha), \quad c=-\tfrac{1}{8}(1-2\alpha), \tag{8}$$

depending only on the filtering parameter α ($\alpha=0.5$ means no filtering). In our simulations a filtering parameter of $\alpha=0.495$ was chosen. Step size variations, presented in a later section, proved that the filter did not influence the flow field in an unphysical manner. Because of the disturbance-flow formulation the filter needs not to be applied to the disturbances.

E. Boundary conditions

1. Free-stream boundary

The boundary conditions at the free-stream boundary are applied in a different manner for the computation of the base flow and the disturbances. The two-dimensional program,

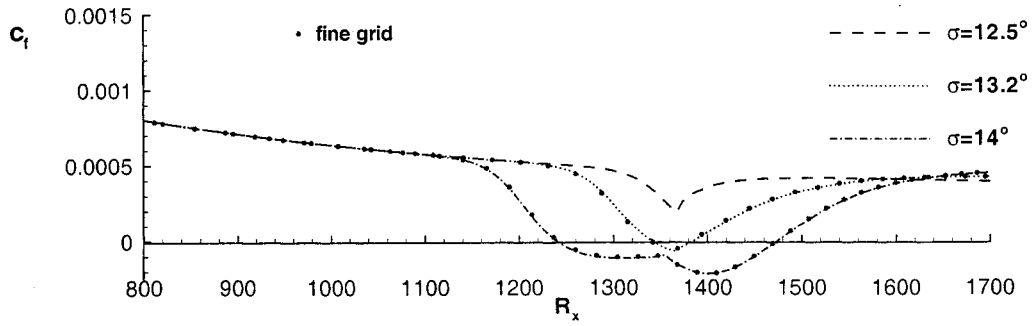

FIG. 2. Skin friction for the cases with shock angles $\sigma=12.5°$, $\sigma=13.2°$, and $\sigma=14°$.

which is used to calculate a steady solution as start-up data for the three-dimensional code, applies a characteristic boundary condition, according to Harris.[22] It assumes that flow variables remain constant along the characteristics in the inviscid potential flow. While this works well for the freestream boundary in the two-dimensional program, it could not be applied to the three-dimensional code. Therefore, a nonreflecting boundary condition[23] is implemented here. The basic idea of this nonreflecting boundary condition is to neglect viscid terms, based on the free-stream assumption. The equations are thus reduced to a hyperbolic problem. Incoming characteristics are then set to zero.

2. Inflow, outflow conditions, wall boundary

The inflow variables are from the compressible boundary layer equations. They are held constant during the simulation. At the outflow boundary, the flow field variables are computed neglecting second derivatives.[18] The no-slip condition and vanishing normal velocity component are assumed at the wall. The disturbance is introduced inside the disturbance strip, according to Fig. 1. It simulates periodical blowing and suction by varying the disturbance quantities $(\rho v)'$, given by a function

$$f_{\rho v}(\xi,z,t)=\hat{a}*\sin(\omega t)*\cos(k\beta z)*\sin(n\xi)*e^{-b\xi^2},\quad -2\pi\leqslant\xi\leqslant 2\pi, \tag{9}$$

with $\xi=\pm 2\pi$ at x_1 and x_2, respectively. In our modal discretization in spanwise direction, k indicates the spanwise Fourier modes, with $k=0$ meaning a two-dimensional disturbance. The disturbance frequency, here ω, determines the streamwise wave number α_r. Thus, the obliqueness angle ψ is given by $\tan\psi=(k\beta)/\alpha_r$. For the present investigations, the wall temperature remains constant. Wall pressure is computed from the v-momentum equation.

3. Initial conditions, implementation of impinging shock wave

At the beginning of the calculation, a laminar flow without impinging shock, given by the boundary layer equations is specified within the whole integration domain. Also at the beginning of the simulation, the shock is introduced into the free-stream boundary. For several grid points upstream from the passage of the shock through the free-stream boundary relevant flow variables are held constant. The variables downstream of the shock location at the free-stream boundary are calculated by the Rankine–Hugoniot relations[17] and also held constant a few gridpoints downstream. A steady shock then establishes itself within the whole flow field during calculation.

III. RESULTS

A. Unperturbed laminar boundary layer

The investigations within this paper are limited to a laminar flat-plate boundary layer with shock boundary layer interaction and Mach number $Ma=4.8$, free-stream temperature $T_\infty=55.4\,\mathrm{K}$ and constant wall temperature $T_w/T_{w,ad}=1$, where $T_{w,ad}$ is the adiabatic wall temperature for the case without shock. The Reynolds-number with respect to the displacement thickness δ^* slightly upstream shock-impingement, but outside the interaction region chosen at $R_x=1100$ is $\mathrm{Re}_{\delta^*,R_x=1100}=12\,546$. For the shock wave, we consider three different shock angles relative to the horizontal axis: $\sigma=12.5°$, $\sigma=13.2°$, and $\sigma=14°$. An earlier validation of the unperturbed flow with impinging shock was performed for $Ma=2$ and adiabatic wall,[14,15] where suitable data have been available. The three different shock angles have been chosen to obtain a flow situation, where the boundary layer is still bound to the plate ($\sigma=12.5°$), a small separation area occurs ($\sigma=13.2°$), and a large separation bubble ($\sigma=14°$) appears. Figure 2 compares the skin friction of the three cases. Separation can be determined by a negative skin friction coefficient c_f. Results for $\sigma=13.2°$ and $\sigma=14°$ based on a finer grid with both half step sizes in streamwise and wall-normal direction are also given in Fig. 2, which prove our solutions as grid independent. It should be pointed out that this statement also includes negligible influence of the filter used, because the filtering spectra depend on the step size as well.

In Fig. 3, density gradients $|\partial\rho/\partial y|$ for $\sigma=14°$ are shown. The largest shock angle σ in our series of computations imposes the highest pressure gradient on the boundary layer, thus forcing a considerable thickening, as well as a large separation bubble, as already seen in Fig. 2. Due to the thickening of the boundary layer and the resulting system of compression and expansion waves, which are typical for such a flow problem,[6] the flow is deflected in a manner which is indicated by some manually placed streamlines in Fig. 3 for the given case.

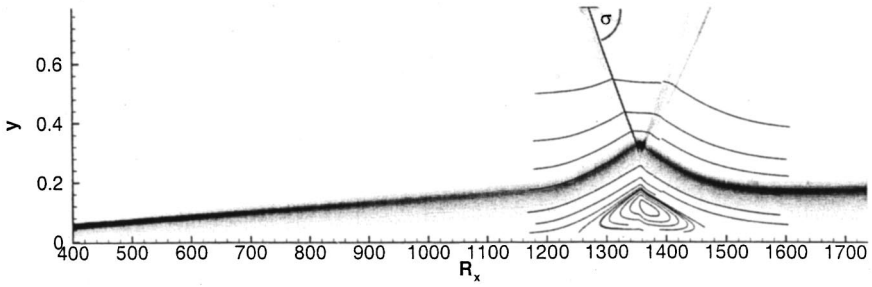

FIG. 3. Density gradients $|\partial\rho/\partial y|$ and selected streamlines for the case with shock angle $\sigma=14°$. Note: y-coordinate stretched by a factor of 11.

B. Linear stability theory

Linear stability theory is used to predict the stability behavior of a boundary layer flow for small amplitude disturbances. In practice, linear stability theory is typically applied under the assumption of a strictly parallel flow, i.e., extracting boundary-layer profiles for $u(y)$ and $T(y)$ for R_x $=$const from the flow field as base-flow profiles for the theory. However, as it will be shown in the following section, nonparallel effects are already considerably large even for a case without impinging shock wave and they can be expected to increase because of the wall-normal velocities induced by the shock boundary layer interaction. More results on this will be shown in the next section.

Figure 4 shows amplification rates $-\alpha_i$ from linear stability theory

$$-\alpha_i=\frac{\partial \ln \dfrac{A(x)}{A_0}}{\partial x}, \tag{10}$$

versus R_x and disturbance frequency

$$F=\frac{2\pi f^* \mu_\infty}{u_\infty^2 \rho_\infty}, \tag{11}$$

where $A(x)/A_0$ is the amplitude ratio of any flow variable and f^* is the dimensional disturbance frequency. Four cases are presented: No shock and the three flow cases with shock impingement as considered above. Darker shadings represent higher amplification rates and the iso-contour line labeled with ''0'' indicates neutral amplification. Drawing our attention to the case without shock in Fig. 4, we see two separated regions of positive amplification. These are, according to Mack,[2] the first instability mode at lower and the second instability mode at higher frequencies, respectively. In the picture for $\sigma=12.5°$ in Fig. 4, the second mode is slightly shifted towards lower frequencies at and near shock impingement, due to the influence of the shock wave. The clear distinction among the first and the second mode is lost. Near shock impingement, only a small, closed area of damping

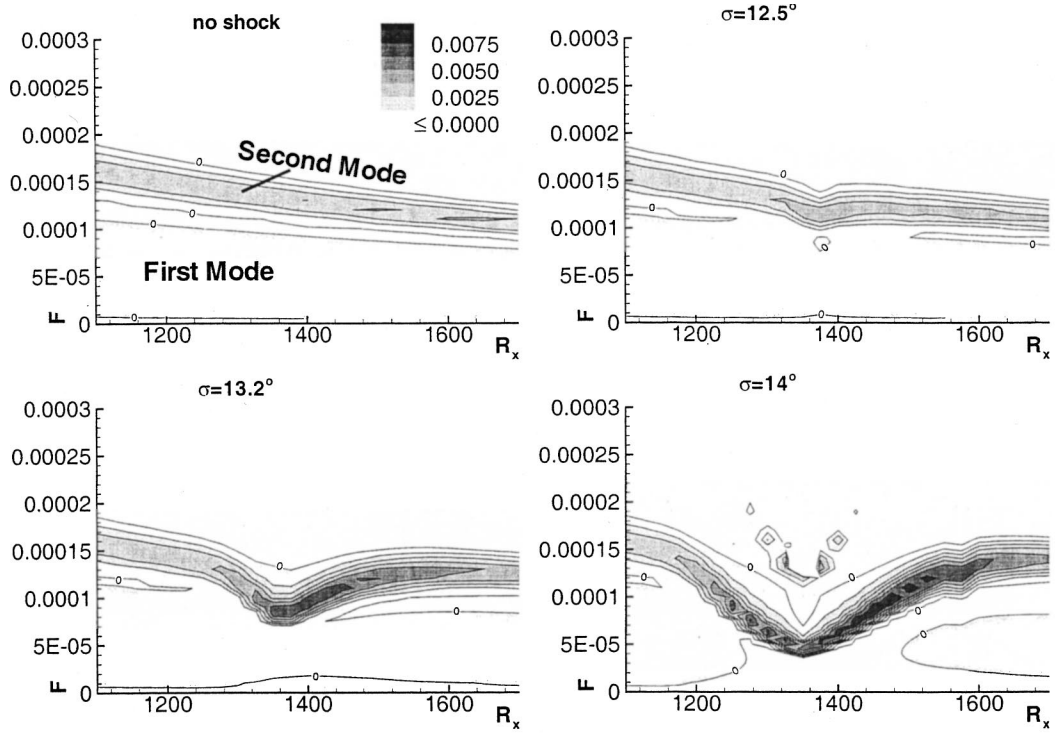

FIG. 4. Linear stability for two-dimensional disturbances and shock angles $\sigma=12.5°$, $\sigma=13.2°$, and $\sigma=14°$ with respect to streamwise direction R_x and frequency F. In the inviscid case, the shock would hit the plate at $R_{x,\mathrm{sh}}\approx 1400$.

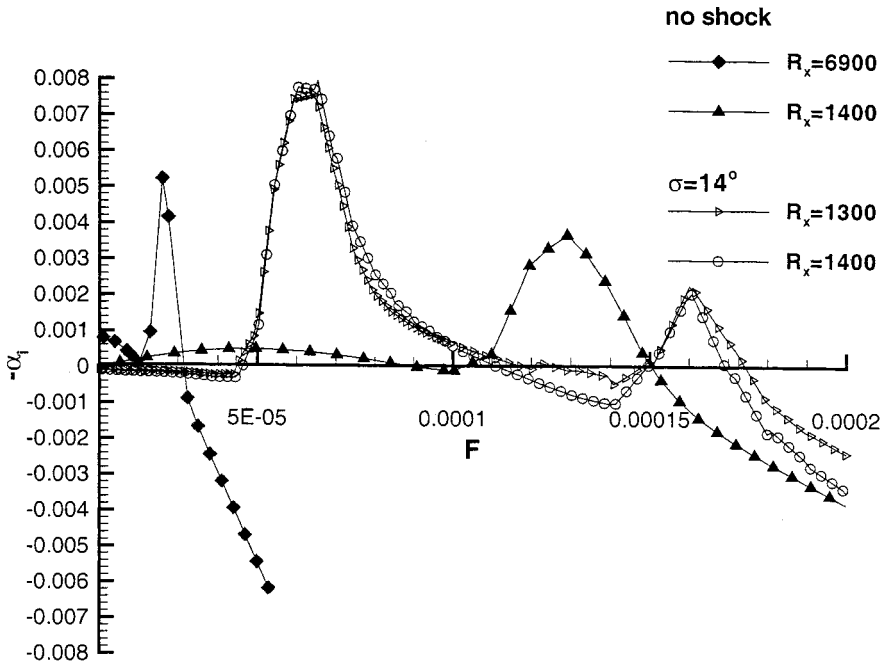

FIG. 5. Amplification rate $-\alpha_i$ vs disturbance frequency F calculated by linear stability theory for the cases without shock and $\sigma=14°$ at different R_x.

remains. The amplification rates at shock impingement and downstream of it increase according to the darker shadings there. A larger shock angle is expected to influence stability behavior to a higher degree. For $\sigma=13.2°$, the observed shift towards lower frequencies and the rise of the amplification rates near shock impingement has become more significant, compared to $\sigma=12.5°$. It is even more pronounced for $\sigma=14°$. Another plainly recognizable effect is the occurrence of new instabilities around the shock impingement area, for frequencies between $F=12*10^{-5}$ and $F=20*10^{-5}$.

Due to the complexity of the behavior of linear disturbances in compressible flows, it can not be expected to relate the phenomena described above to one single factor. Therefore, we try to explain the influence of the shock wave on the linear stability by taking a closer look at various effects and what sort of behavior has to be expected for both first and higher mode instabilities. First, we investigate the influence of viscosity. Figure 5 shows the amplification rate versus the disturbance frequency for linear stability calculations of boundary layers with and without shock at different locations R_x. Comparing the cases without shock at $R_x=1400$ and $R_x=6900$ (filled symbols), the effect of viscosity becomes obvious. For the curve at $R_x=1400$, maximum amplification rates for both first and second mode disturbances (second mode disturbances are located at higher disturbance frequencies) are smaller than the corresponding values for $R_x=6900$, indicating a stabilizing effect of viscosity at higher Mach numbers, as mentioned in the Introduction.

The shock wave with $\sigma=14°$ forces the boundary layer to separate and the separation bubble displaces the boundary layer away from the wall. In a simplified manner this could be understood as an increase of the local Reynolds number R_x, because $R_x \sim \delta$, with δ as the boundary layer thickness. An infinite local Reynolds number corresponds to an inviscid flow. Therefore, the influence of viscosity decreases with increasing displacement of the boundary layer. In the present Mach number range, viscosity has a destabilizing effect on the stability of the boundary layer. The amplification curves for the case with a shock angle of $\sigma=14°$ are given in Fig. 5 at $R_x=1300$ and $R_x=1400$ (open symbols). The maximum amplification rate becomes even larger than the corresponding amplification rate at $R_x=6900$ without shock. It can thus be stated that the displacement of the boundary layer, which results in a diminishing of the influence of viscosity, leads to a destabilization, but it can not be accounted for the total rise in amplification. The unstable region around $F=16\cdot 10^{-5}$ belongs to the new instabilities mentioned before.

Figure 6 compares streamwise velocity profiles and their characteristics $u(\eta)\pm a(\eta)$ at five consecutive locations R_x with the corresponding phase velocity c_{ph} of a disturbance. For $\eta<\eta_s$ the disturbance wave propagates at supersonic speed relative to the flow because $u(\eta)+a(\eta)<c_{\mathrm{ph}}$, where $u(\eta)$ is the streamwise velocity component and $a(\eta)$ the local speed of sound. Mack pointed out, that the amplification rate of second-mode instabilities is strongly dependent on the thickness of such local regions of relative supersonic flow. The figures shows, that the thickness η_s of relative supersonic flow increases by the presence of separation until a maximum at $R_x\approx 1350$ is reached. Hence, another portion of the total rise of second mode instability can be assumed to be caused by the increase of thickness in this local supersonic regions.

Although the first-mode instability in Fig. 4 seems to vanish locally with increasing shock strength, a first-mode instability has to be present, according to the findings by Lees and Lin,[3] because a generalized inflection point exists (see Fig. 7). The location of the generalized inflection point in Fig. 7 moves in wall-normal direction due to the displacement of the boundary layer by the separation bubble.

Figure 8 shows amplification rates for a frequency $F=10*10^{-5}$, but different shock angles and propagation angles of the disturbance waves ψ with respect to the stream-

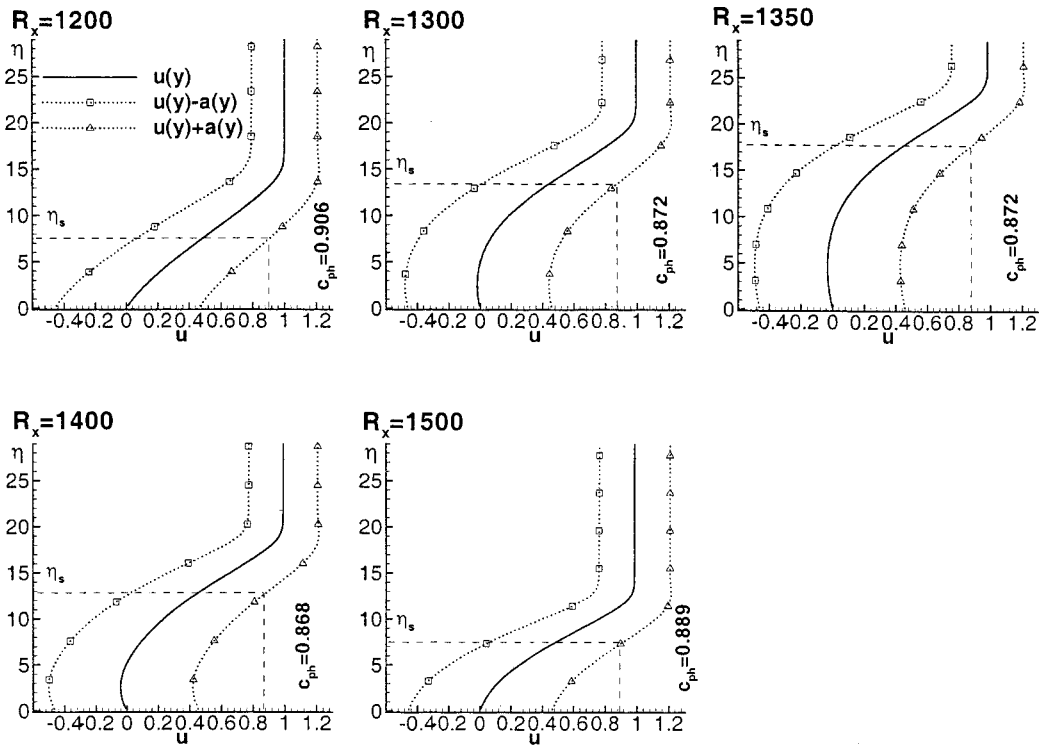

FIG. 6. Velocity profiles and their characteristics at five consecutive locations R_x. Also, corresponding phase velocities c_{ph} of a disturbance with $F=1\cdot10^{-4}$ are given. Shock angle $\sigma=14°$.

wise direction. For $\psi=0°$, which corresponds to a two-dimensional disturbance, the maximum amplification rate is raised by a factor of ≈30. For $\psi=25°$, this factor is ≈60, while for $\psi=45°$, the amplification rate grows by a factor of ≈6. Ahead of the high local rise for $\sigma=14°$ it can be seen that $-\alpha_i$ adopts negative values, indicating that small disturbances are damped here, which compensates the rise of $-\alpha_i$ to a certain degree. In summary, for linear stability theory an impinging shock wave locally influences the stability behavior of a boundary layer considerably. This influence depends

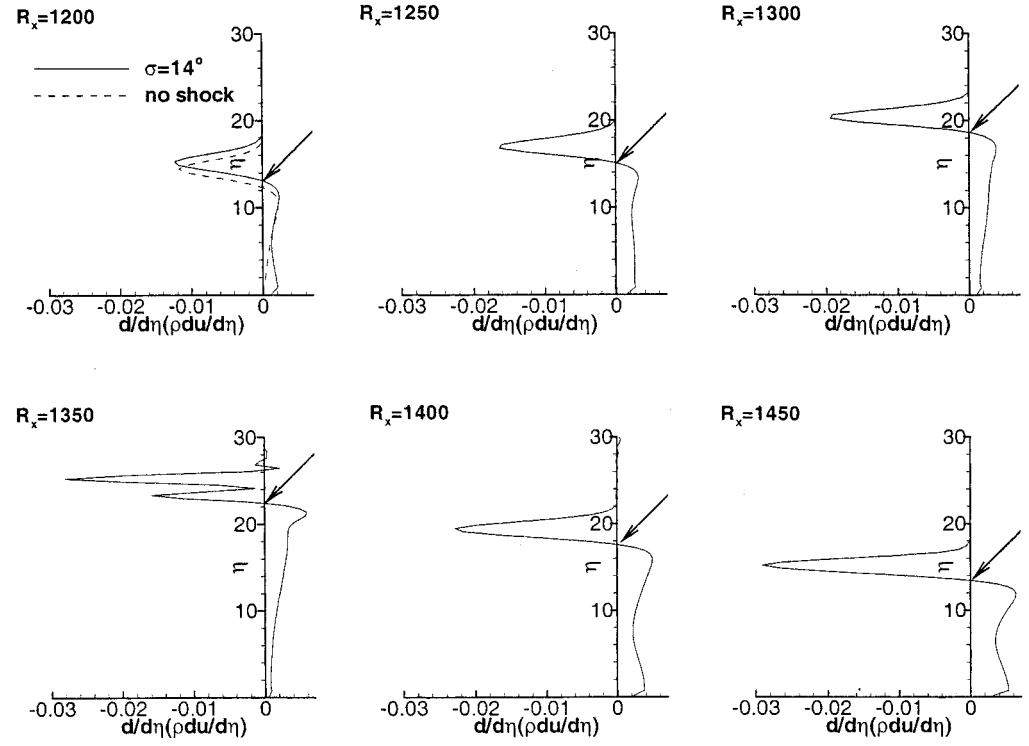

FIG. 7. Location of generalized inflection point $\mathbf{d}(\rho\mathbf{du}/\mathbf{d}\eta)\mathbf{d}\eta=\mathbf{0}$ for the case $\sigma=14°$ (solid line) and without shock (broken line) at different R_x.

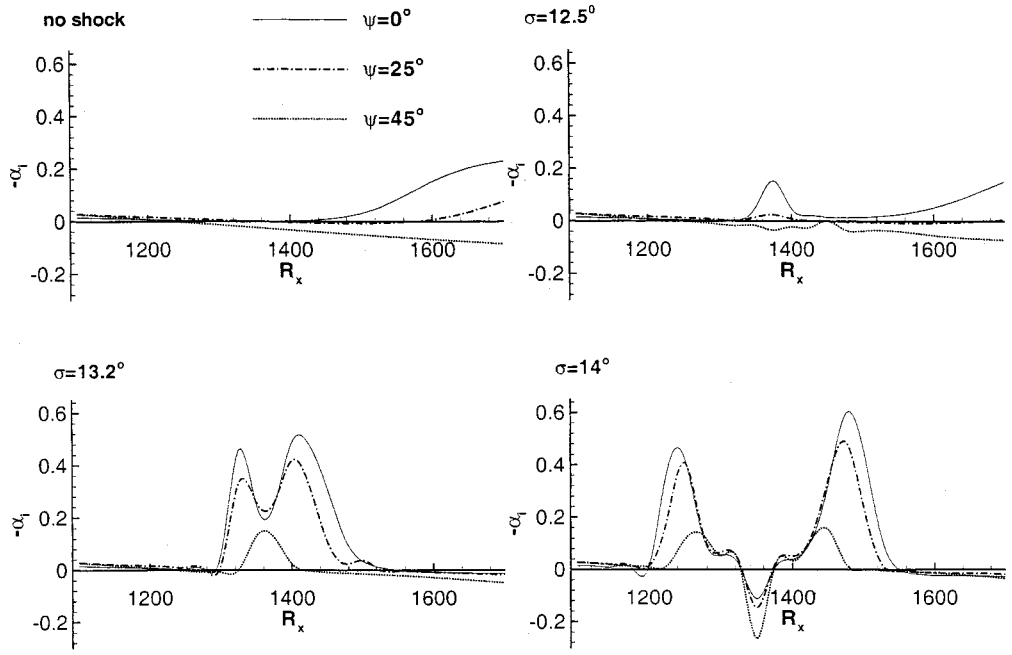

FIG. 8. Amplification rates by linear stability theory for $\sigma=12.5°$, $\sigma=13.2°$, and $\sigma=14°$. Disturbance frequency is $F=1\cdot10^{-4}$, propagation angles of disturbance waves with respect to the x direction are $\psi=0°$, $\psi=25°$, and $\psi=45°$.

on the shock angle σ, the wave angle ψ with respect to the x direction and the disturbance frequency F. The larger the shock angle σ, the higher the local influence and the larger the area of influence with respect to the streamwise direction.

C. Direct numerical simulations and comparison with linear stability theory

In the present section we focus on results which were obtained by direct numerical simulations (DNS). Periodical disturbances are introduced at the disturbance strip. During simulation these travel downstream through the interaction region and finally into the buffer domain at outflow. Simulations are carried out until a periodical disturbance structure is present inside the integration domain. The flow field is then analyzed. In order to better understand the following results with a shock, we first draw our attention to a case without impinging shock wave. Figure 9 shows amplification rates obtained by extracting different disturbance maxima from the amplitudes of a timewise Fourier transform for one disturbance period of such a simulation. The disturbance frequency is given in the plot, the other simulation parameters correspond to those used in earlier sections. In addition, results of linear stability theory, as well as results of a simulation based on an idealized parallel boundary layer at three consecutive locations R_x are given. A typical nonparallel effect is the individual amplification rate for each flow-field variable. In contrast to this, linear stability theory yields one single amplification rate as long as it is based on a strict parallel flow assumption as mentioned before. To prove that the differences between the flow variables of the numerical simulation and the differing amplification rates between linear stability theory and simulation are caused by nonparallel effects, the code has been modified to simulate stability behavior at three consecutive locations based on an idealized, parallel base flow. As it can be seen in Fig. 9, thus obtained results agree very well with linear stability theory. Systematically, near-wall amplification rates such as amplification rates obtained from the maximum disturbance amplitudes of u, v, and p (of which only the wall pressure is shown in Fig. 9) tend to be farther from the calculated values by linear theory than wall distant maxima (T, ρ, and for three-dimensional disturbances w).

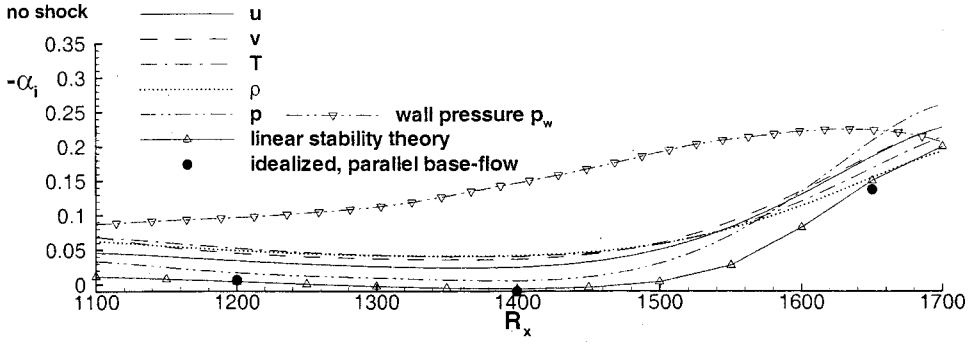

FIG. 9. Amplification rates of wall distant disturbance maxima and wall pressure by direct numerical simulation, compared with linear stability theory and an idealized parallel-flow simulation; disturbance frequency $F=1\cdot10^{-4}$; no shock.

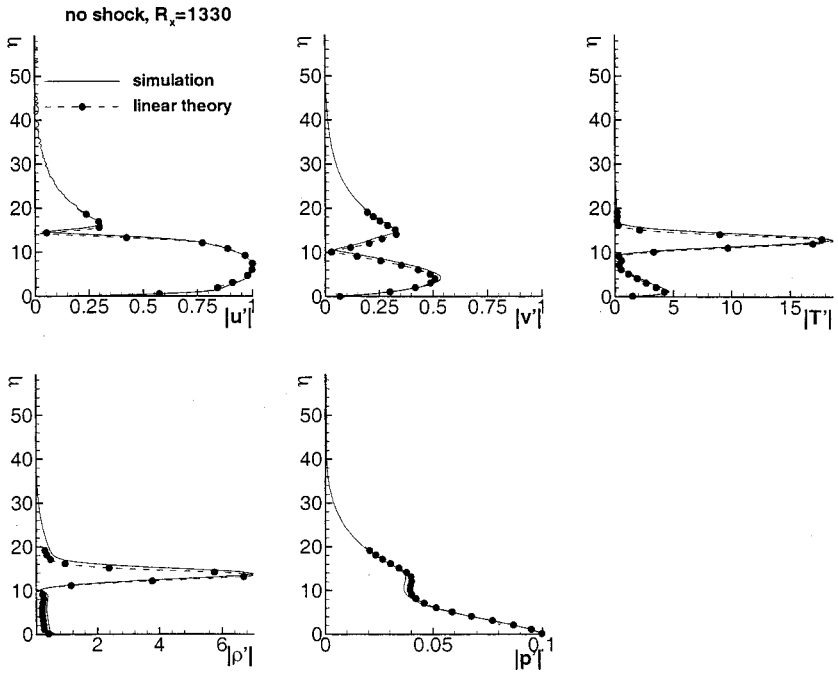

FIG. 10. Amplitude distributions of relevant flow variables compared with linear stability theory at $R_x=1330$. Disturbance frequency is $F=1\cdot10^{-4}$.

Figure 10 compares disturbance amplitudes from the direct numerical simulation with eigenfunctions of linear stability theory for some flow variables at $R_x=1330$ without impinging shock. Phase angles for the same case are compared in Fig. 11. Having the differences between linear stability theory and direct numerical simulation observed earlier in this section in mind, they agree remarkably well.

We now move on to take a closer look at the stability behavior of small amplitude disturbances in flow situations with shock boundary layer interaction, simulated by DNS. First, the case with a relatively small shock angle of $\sigma=12.5°$ is investigated, for which a smaller influence of the shock wave on the disturbance amplification can be expected (cf. Fig. 2). Figure 12 shows maximum disturbance amplitudes for all relevant flow variables. Here, disturbances are two-dimensional. Along with the results of DNS with impinging shock wave, data of a DNS without shock as well as corresponding curves from linear stability theory are given.

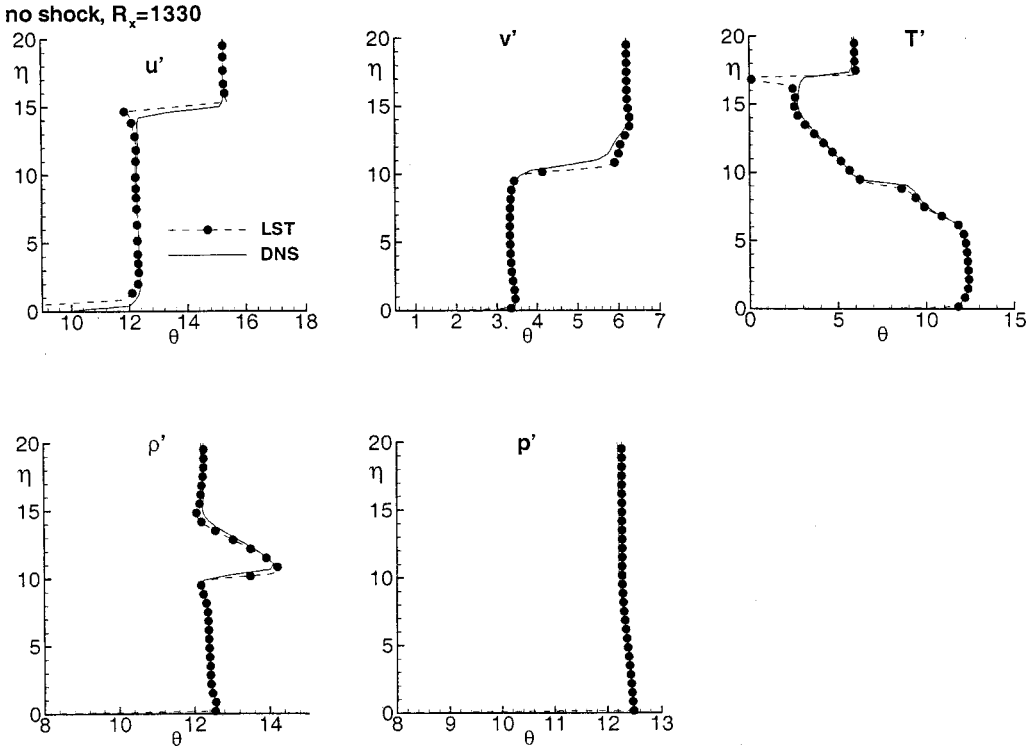

FIG. 11. Phase angles Θ of relevant flow variables compared with linear stability theory at $R_x=1330$. Disturbance frequency is $F=1\cdot10^{-4}$.

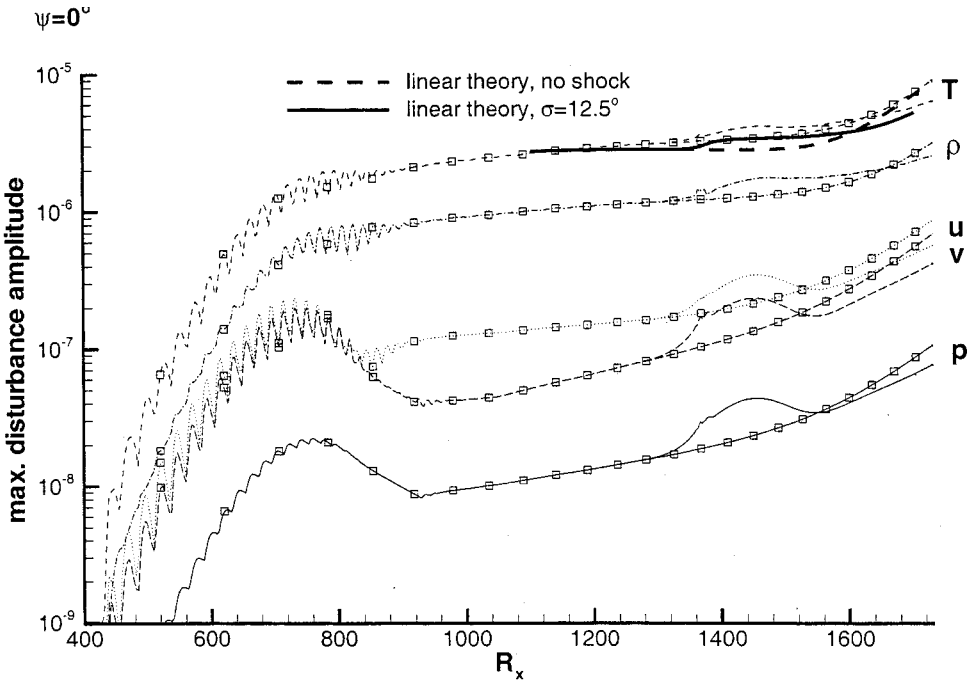

FIG. 12. Maximum disturbance amplitudes of flow variables for a shock angle of $\sigma=12.5°$ compared to the case without shock and linear stability theory. Two-dimensional disturbances ($\psi=0°$), disturbance frequency $F=1\cdot10^{-4}$.

As with the nonparallel effects, the influence of the shock wave on the stability behavior is significantly different for each individual flow field variable. Like in the case without shock, linear stability theory lies in better accordance with wall distant maxima such as temperature T or density ρ. Comparing the two base flow cases "with and without shock" to the corresponding results of linear theory, we see that in both cases the difference between the predicted curve of the disturbance amplitude by linear stability theory is the same. This difference can thus be identified as the already presented nonparallel effects, as discussed before. Hence, it can be stated that linear stability theory as it is applied here

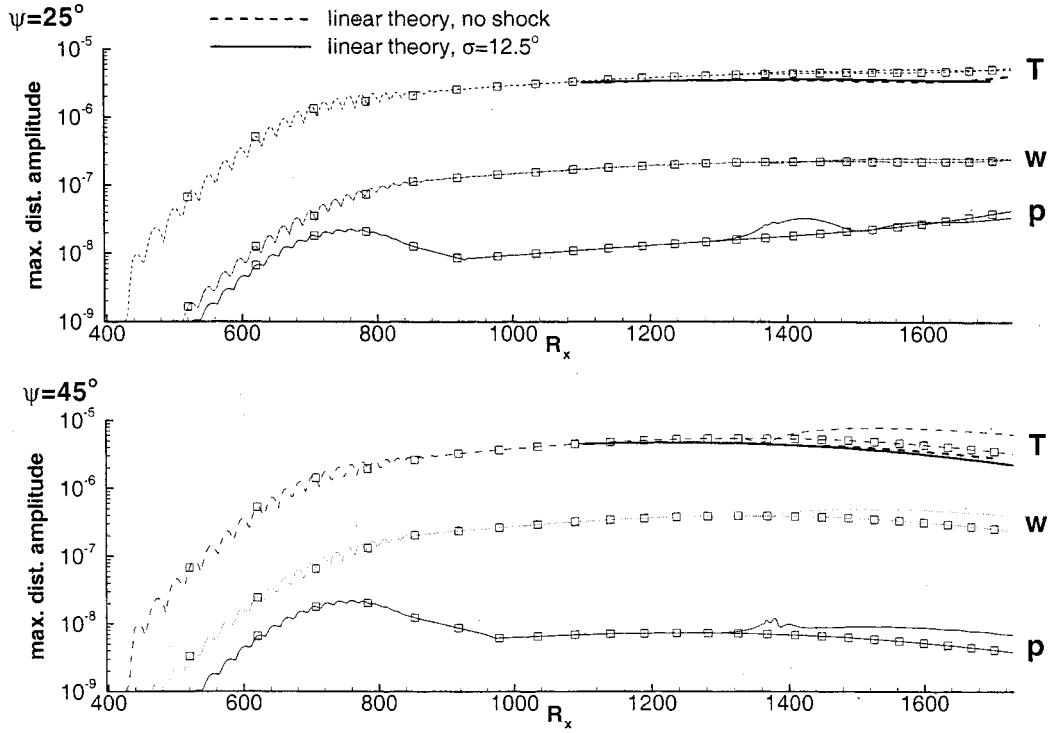

FIG. 13. Maximum disturbance amplitudes of selected flow variables for a shock angle of $\sigma=12.5°$ compared to the case without shock and linear stability theory. Propagation angles of disturbance waves with respect to the x direction $\psi=25°$ and $\psi=45°$, disturbance frequency is $F=1\cdot10^{-4}$.

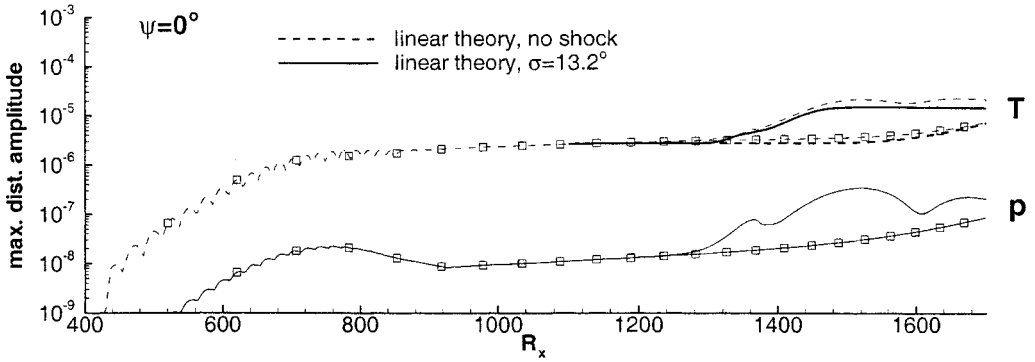

FIG. 14. Maximum disturbance amplitudes of flow variables p and T for a shock angle of $\sigma=13.2°$ compared to the case without shock and linear stability theory. Two-dimensional disturbances ($\psi=0°$), disturbance frequency $F=1\cdot10^{-4}$.

is qualitatively able to predict disturbance amplitude behavior for wall-distant maxima of flow variables. However, close to the wall, where u, v, and p maxima are located, the nonparallel results exhibit a local increase of the disturbances in the vicinity of the impinging shock which is not present in the linear stability theory results. The same is valid for three-dimensional disturbance waves ($\psi=25°$ and $\psi=45°$) in Fig. 13, where disturbance amplitudes of temperature T, pressure p, as well as the disturbance velocity component in spanwise direction w are shown. The w maximum is located in a farther position normal to the wall, close to the temperature maximum. The rise of the disturbance amplitudes for oblique waves is much smaller than in the two-dimensional case in Fig. 12. Linear stability theory predicts only a small rise compared to the boundary layer without impinging shock. Again, the influence of the shock is most pronounced at near-wall amplitude maxima, such as p, which is located directly at the wall. For $\psi=45°$ linear stability theory does not predict the correct behavior. Instead of an additional amplification, it predicts a minor damping. For a boundary layer with no impinging shock it is known, that by increasing the angle ψ of the disturbance propagation with respect to the x direction, results of linear stability theory exhibit increasing nonparallel effects.

In the case presented in Fig. 14 the shock angle is increased to $\sigma=13.2°$. Temperature and pressure maxima are plotted as representatives of wall-distant disturbances and disturbances, which are close to the wall for comparison to the case without shock boundary layer interaction and linear stability theory. Compared to $\sigma=12.5°$ disturbance amplitudes increase much stronger by the interaction. For the wall-distant amplitudes linear stability theory quantitatively works rather well. This is not true for the pressure disturbance at the wall, as before. Downstream of the shock impingement at $R_x\approx1500$ wall-pressure amplitudes are damped until $R_x\approx1600$, where damping is followed by another amplification. A closer investigation of this phenomenon revealed neither a beating of waves nor a nonphysical problem such as numerical reflections from the free-stream or outflow boundary.

Figure 15 shows the wave number distribution $\alpha_r=2\pi/\lambda$ of the DNS for the wall pressure disturbance and a fixed frequency $F=10\cdot10^{-5}$. The wave number can be regarded as a measure for the wave propagation speed c_r, because of $c_r=F/\alpha_r$. Hence, at shock impingement and a certain area upstream of it, the disturbance wave is decelerated by the shock, downstream shock impingement, it is accelerated. The area of alternating amplification and damping at $R_x\approx1600$ discussed above can be correlated to a deceleration and acceleration of the wave propagation represented in Fig. 15 as a local increase followed by a decrease of the wave number α_r, respectively. As stated before, this occurrence cannot be related to an external effect.

Amplitude profiles normal to the wall and phase angles for the case with $\sigma=13.2°$ and $\psi=0°$ at $R_x=1325$, which is a position just before shock impingement, show fairly good agreement with eigenfunctions and phase angles calculated by linear stability theory. The now larger nonparallel effects are expected to impair the agreement between DNS and linear stability theory, which effectively is the case here. For three-dimensional disturbance waves ($\psi=25°$ and $\psi=45°$) the match between linear stability theory and DNS for wall

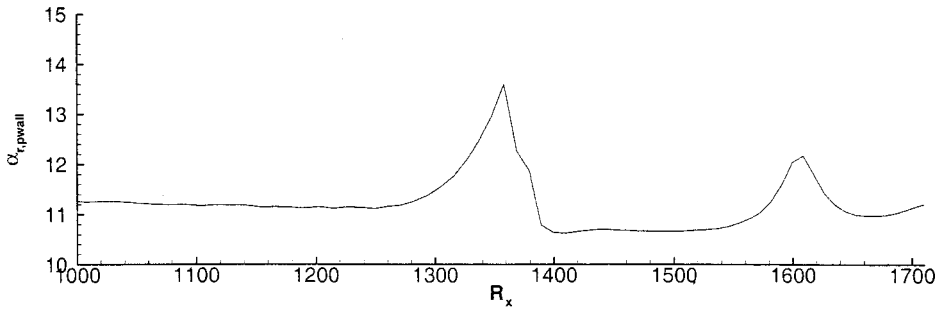

FIG. 15. Wave number distribution α_r from direct numerical simulation for disturbance frequency $F=1\cdot10^{-4}$ and a shock angle $\sigma=13.2°$. Two-dimensional disturbances ($\psi=0°$).

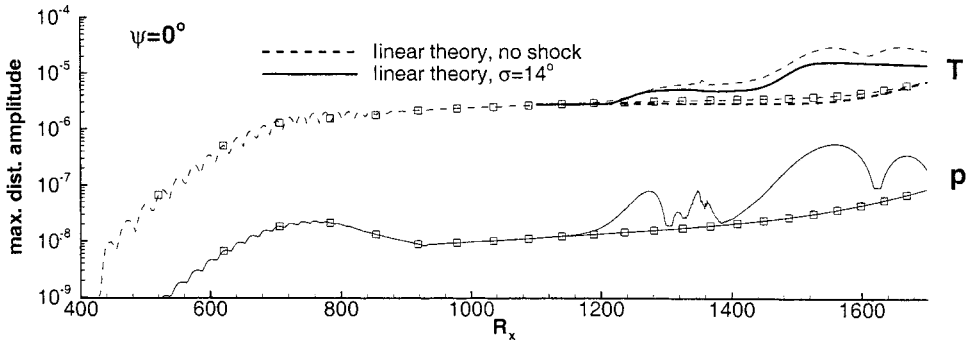

FIG. 16. Maximum disturbance amplitudes of flow variables p and T for a shock angle of $\sigma=14°$ compared to the case without shock and linear stability theory. Two-dimensional disturbances ($\psi=0°$), disturbance frequency $F=1\cdot10^{-4}$.

distant amplitude maxima is slightly better than for $\sigma=12.5°$.

Finally, we discuss the case with the largest separation bubble produced by a shock angle of $\sigma=14°$. Results are presented in Fig. 16 and are again compared with linear theory. Although non-parallel effects are expected to grow with increasing shock angles, the tendency of the disturbance amplitudes of wall-distant maxima can be predicted fairly good by linear theory. After a rise of the amplitude maxima near separation, the temperature disturbance amplitude remains almost constant within the separation bubble. At reattachment another rise in amplitude maxima occurs. The total amplitude rise here is not significantly higher than for $\sigma=13.2°$, however.

Amplitudes and phase angles are compared with linear stability theory in Fig. 17 at $R_x=1250$, a location slightly upstream from shock impingement. Quantitatively, the trend of the curves of the simulation can be represented by results of linear theory, although nonparallel effects grow in magnitude. Figure 18 shows maxima of disturbance amplitudes for $\psi=25°$ and $\psi=45°$. As for the other cases discussed earlier the agreement between linear theory and DNS is best for $\psi=0°$ but declines with increasing obliqueness angle ψ.

IV. CONCLUSIONS AND FUTURE RESEARCH

We could identify considerable nonparallel effects for a boundary layer at $Ma=4.8$ with respect to small-amplitude disturbance behavior, even for a boundary layer without impinging shock wave. Linear stability theory according to Mack could represent linear stability behavior for wall-distant amplitude maxima and small propagation angles ψ of disturbance waves rather well despite these nonparallel effects. An impinging shock wave thus locally influences stability behavior, dependent on the shock strength, disturbance frequency and obliqueness angle ψ of traveling disturbances. The influence can be explained by an interaction of several factors. First, decreasing viscosity effects due to the displacement of the boundary layer away from the wall are responsible for a certain rise in instability, because at higher Mach numbers viscosity has a known stabilizing effect. Also, local

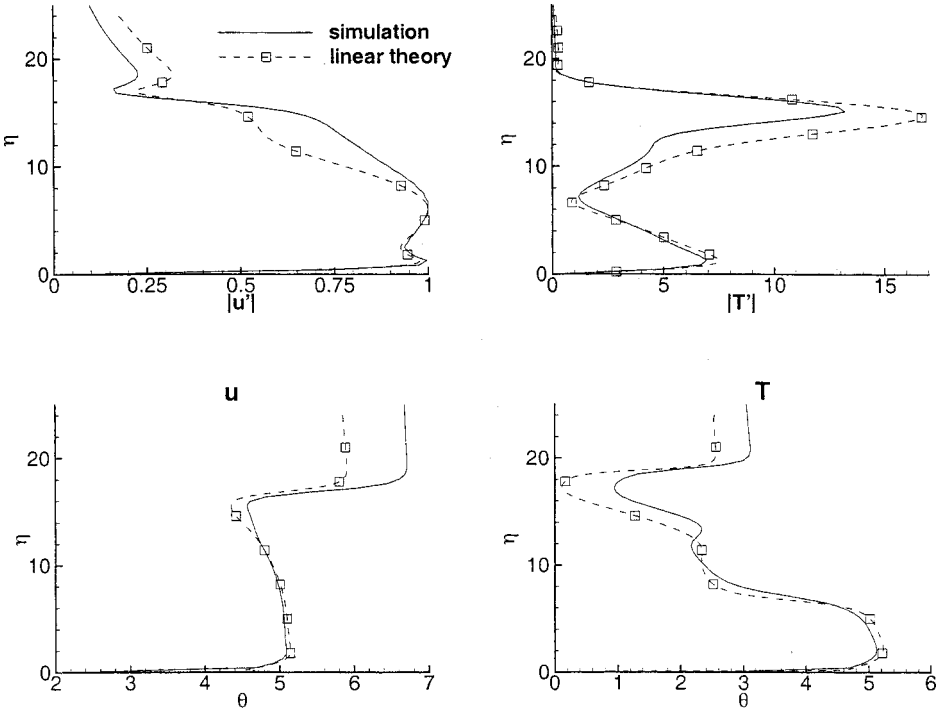

FIG. 17. Comparison of amplitude distributions of numerical simulation with eigenfunctions of linear stability theory and corresponding phase angles for selected variables at $R_x=1250$. Shock angle $\sigma=14°$ and propagation angles of disturbance waves with respect to the x direction $\psi=0°$. Disturbance frequency is $F=1\cdot10^{-4}$.

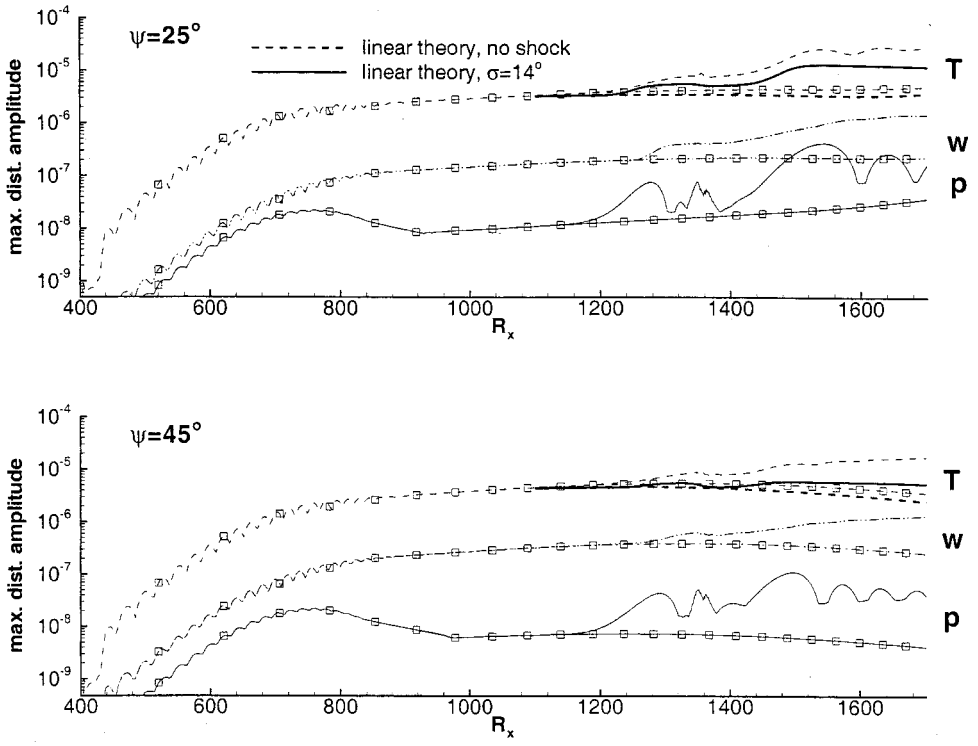

FIG. 18. Maximum disturbance amplitudes of flow variables T, w, and p for a shock angle of $\sigma=14°$ compared to the case without shock and linear stability theory. Propagation angles of disturbance waves with respect to the x direction $\psi=25°$ and $\psi=45°$, disturbance frequency is $F=1\cdot10^{-4}$.

relative supersonic zones become thicker within the region where the boundary layer thickens. This is known to promote second-mode instability.

Future research will be carried out for secondary instability mechanisms such as fundamental, subharmonic or oblique breakdown, also for stronger shocks and higher Mach numbers which eventually cause an unsteady flow field. This implies modifications of the numerical scheme. Another issue is the sensitivity with respect to more complicated wall conditions like adiabatic or radiation–adiabatic wall temperatures. First simulations at $Ma=4.8$ and adiabatic wall condition did not deliver considerable differences compared to calculations with constant wall temperature, because the constant wall temperature chosen here is identical to the adiabatic wall temperature of the corresponding boundary layer without shock. The shocks investigated here resulted only in slight changes of the adiabatic wall temperature on the order of $\Delta T=5$ K. A higher Mach number and stronger shock waves are, therefore, desirable in this case, too.

ACKNOWLEDGMENT

The authors would like to thank the Deutsche Forschungsgemeinschaft for supporting this research within Sonderforschungsbereich 259.

[1]W. Saric, E. Reshotko, and D. Arnal, "Hypersonic laminar-turbulent transition," AGARD AR-319 (1998).
[2]L. Mack, "Boundary layer stability theory," Jet Propulsion Laboratory, Pasadena, Tech. Rep. 900-277 (1969).
[3]L. Lees and C. Lin, "Investigation of the compressible laminar boundary layer," NACA Tech. Note 1115 (1946).
[4]J. Ackeret, F. Feldmann, and N. Rott, Report no. 10, ETH Zürich, Institut für Aerodynamik, 1946.
[5]H. Liepmann, "The interaction between boundary layer and shock waves in transsonic flow," J. Aeronaut. Sci. **13**, 623 (1946).
[6]J. Délery and J. Marvin, "Shock-wave boundary layer interactions," AGARDograph 280 (1986).
[7]J. Délery, "Shock phenomena in high speed aerodynamics: Still a source of major concern," Aeronaut. J. **103**, 19 (1999).
[8]D. Dolling, "Fifty years of shock-wave/boundary-layer interaction research: What next?" AIAA J. **39**, 1517 (2001).
[9]A. Thumm, Dissertation, Universität Stuttgart, 1991.
[10]W. Eißler, Dissertation, Universität Stuttgart, 1995.
[11]W. Eißler and H. Bestek, "Spatial numerical simulations of linear and weakly nonlinear wave instabilities in supersonic boundary layers," Theor. Comput. Fluid Dyn. **8**, 219 (1996).
[12]W. Eißler and H. Bestek, "Direct numerical simulation of transition in Mach 4.8 boundary layers at flight conditions," *Engineering Turbulence Modelling and Experiments*, edited by W. Rodi and G. Bergeles (Elsevier, New York, 1996), Vol. 3, pp. 611–620.
[13]A. Fezer and M. Kloker, "Transition process in Mach 6.8 boundary layers at varying temperature conditions investigated by spatial direct numerical simulation," *Notes on Numerical Fluid Mechanics* (Vieweg, New York, 1999), Vol. 72, pp. 138–145.
[14]A. Pagella, Master Thesis, Universität Stuttgart, 1999.
[15]A. Pagella, U. Rist, and S. Wagner, "Numerical investigations of small-amplitude disturbances in a laminar boundary layer with impinging shock waves," *Notes on Numerical Fluid Mechanics* (Springer, New York, 2001), Vol. 77, pp. 146–153.
[16]H. Schlichting, *Boundary-Layer Theory*, 7th ed. (McGraw-Hill, New York, 1979), pp. 328–330.
[17]J. Anderson, Jr., *Modern Compressible Flow* (McGraw-Hill, New York, 1990), pp. 104–108.
[18]M. Kloker, U. Konzelmann, and H. Fasel, "Outflow boundary conditions for spatial Navier–Stokes simulations of transition boundary layers," AIAA J. **31**, 620 (1993).
[19]M. Kloker, "A robust high-resolution split-type compact FD scheme for spatial direct numerical simulation of boundary-layer transition," Appl. Sci. Res. **59**, 353 (1998).

[20]S. Orszag, ''Numerical simulation of incompressible flows within simple boundaries. I. Galerkin (spectral) representations,'' Stud. Appl. Math. **L**, 293 (1971).
[21]S. Lele, ''Compact finite difference schemes with spectral-like resolution,'' J. Comput. Phys. **103**, 16 (1992).
[22]P. Harris, Dissertation, University of Arizona, 1993.
[23]K. Thompson, ''Time dependent boundary conditions for hyperbolic systems,'' J. Comput. Phys. **68**, 1 (1987).